Article

Chemically Modified Electrodes Based on 4-((5-Isopropyl-3, 8-dimethylazulen-1-yl)methylene)-2-phenyloxazol-5(4H)-one

Alina-Giorgiana Brotea [1], Ovidiu-Teodor Matica [1], Cornelia Musina (Borsaru) [1], Andreea Madalina Pandele [2], Roxana Trusca [1] and Eleonora-Mihaela Ungureanu [3,*]

[1] Faculty of Chemical Engineering and Biotechnologies, National University of Science and Technology Politehnica Bucharest, Gh. Polizu 1-7, Sector 1, 011061 Bucharest, Romania; alina.brotea@stud.chimie.upb.ro (A.-G.B.); ovidiu.matica@stud.chimie.upb.ro (O.-T.M.); cornelia.musina@stud.chimie.upb.ro (C.M.); roxana_doina.trusca@upb.ro (R.T.)

[2] Advanced Polymer Materials Group, University Politehnica of Bucharest, Gh. Polizu 1-7, 011061 Bucharest, Romania; madalina.pandele@upb.ro

[3] Doctoral School of Chemical Engineering and Biotechnologies, National University of Science and Technology Politehnica Bucharest, Gh. Polizu 1-7, Sector 1, 011061 Bucharest, Romania

* Correspondence: mihaela.ungureanu@upb.ro

Abstract: Novel chemically modified electrodes (CMEs) based on azulene were prepared by electrooxidation of guaiazulene derivative 4-((5-isopropyl-3,8-dimethylazulen-1-yl)methylene)-2-phenyloxazol-5(4H)-one (**G**). **G** is based on guaiazulene non-alternating aromatic hydrocarbon exhibiting a less symmetrical structure compared to naphthalene skeletal derivative. Therefore, it can be used as a building block for the preparation of novel materials. To evaluate the chemical structure and surface images, the CMEs based on **G** (**G**-CMEs) were characterized by ferrocene redox probe, X-ray photon spectroscopy (XPS), and scanning electron microscopy (SEM). They were also tested for the analysis of synthetic samples of heavy metal (HM) ions. The influence of preparation conditions (electric charge and potential) on the properties of these CMEs was examined. This paper highlights the importance of electropolymerization conditions on electrodeposited film surfaces, especially on their analytical properties vs. Cd(II), Pb(II), Cu(II), and Hg(II) investigated ions. This study is relevant for further design and development of advanced materials based on azulenyl-phenyloxazolone for the HM analysis in water. A linear dependence of the peak currents for Pb(II) ion on the concentration in test aqueous solutions was obtained between 10^{-7} M and $5 \cdot 10^{-5}$ M. The detection limits of $5 \cdot 10^{-6}$ M; 10^{-7} M; $5 \cdot 10^{-6}$ M; and 10^{-5} M were estimated for Cd(II), Pb(II), Cu(II), and Hg(II), respectively, for **G**-CMEs.

Keywords: 4-((5-isopropyl-3,8-dimethylazulen-1-yl)methylene)-2-phenyloxazol-5(4H)-one; voltammetric methods; XPS; SEM; HM analysis

1. Introduction

The CMEs based on oxazolones may be considered promising tools for heavy metals (HMs) analysis due to the presence of an oxazolone complexing group, which can be grafted on the electrode surface. In our group, for the first time, modified electrodes based on 2-phenyl-4-((4,6,8-trimethylazulen-1-yl)methylene)oxazol-5(4H)-one (**M**) were prepared by electrochemical methods [1]. Their tests for heavy metal analysis indicated good results for Pb(II) recognition using this type of ligand. Their study through voltammetric methods, EIS, SEM, and XPS evidenced that the main parameters that control the analytical performances are the electropolymerization potential and electric charge. However, their detection limit was not low enough. At the same time, it is known that the structure of the ligand can be particularly important in the analytical responsiveness of the modified electrode [2]. Therefore, similar ligands from the azulenyl-phenyloxazolone class are the subject of our

current investigation. Their preparation involves the in-depth electrochemical study of the ligands to establish the electrochemical processes they can undergo.

The results of the electrochemical investigation on 4-((5-isopropyl-3,8-dimethylazulen-1-yl)methylene)-2-phenyloxazol-5(4H)-one (**G**) are presented in this paper. The oxazolone ring (colored in red) from its structure (Figure 1) is recognized for its complex properties in relation to HMs [3]. This compound belongs to five-membered rings containing nitrogen and oxygen heteroatoms that are "masked" amino acids [4–8]—versatile structures for many organic syntheses. The investigated compound is interesting because its electrochemical properties are similar to novel organic electronic materials [9–13].
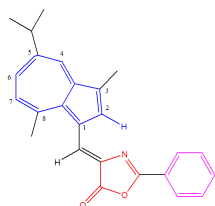

Figure 1. Structure of 4-((5-isopropyl-3,8-dimethylazulen-1-yl)methylene)-2-phenyloxazol-5(4H)-one (**G**).

The structure of this guaiazulene ligand contains also a phenyl ring in position two (colored in magenta), which is linked by a C=C bond to guaiazulene (azulene—colored in blue and substituted with isopropyl and two methyl groups). The electrochemical properties of **G** were related to those of the modified electrodes built from **G**.

G belongs to the class of azulene, non-alternating aromatic hydrocarbons [14], which have low ionization energy, high electron mobility, and less symmetrical structure compared to structural isomers from naphthalene. Azulene gives the **G** molecule special chemical and physical properties that can be the basis for the preparation of smart materials with valuable technical properties [15–20].

Previous research on such azulene compounds has demonstrated that azulene-based monomers are promising compounds for the construction of modified electrodes designed for the detection of HMs [21]. The presence of the azulenyl moiety (able to undergo anodic polymerization) and the oxazol-5(4H)-one functional group (with high affinity for cations) leads to a higher electron density of this second group and, consequently, to push-pull structures useful to build complexing modified electrodes [22]. Another interest in the study of this compound is its potential response in NLO or coloring properties [23,24]. Several azulenyl-phenyloxazolones were investigated for their optical properties [14,21]. Their encouraging performance stimulated our interest in studying **G** among other oxazolones. After the electrochemical study, polymerization tests were carried out in order to obtain new CMEs based on azulenes. The obtained CMEs were studied using ferrocene redox probe, and their surface was examined by XPS and SEM following similar approaches to those recently published [25]. They were also tested as sensors for the analysis of HMs.

2. Materials and Methods

G was synthesized by condensation of the hippuric acid derivative with azulene-1-carbaldehyde [21]. The main features of **G** were checked: crystalline state, melting point (m.p.), UV-Vis wavelength (λ), and the corresponding extinction coefficient on the logarithmic scale (log ε) from the spectra recorded in methanol, chemical shifts for the ^{1}H-NMR, and ^{13}C-NMR peaks recorded in deuterated chloroform—singlet (s), doublet (d), triplet (t), and their coupling constant (J); IR wavelengths and their intensity—weak (w), medium (m), strong (s), very strong (vs); and mass spectrum (MS) and elemental analysis calculated and found for $C_{25}H_{23}NO_2$ (see the Supplementary Material).

High-purity acetonitrile (CH_3CN) (Sigma Aldrich, electronic grade 99.999% trace metals) was used as a solvent. For the supporting electrolyte, tetrabutylammonium perchlorate (TBAP, Fluka, Munich, Germany, analytical purity $\geq$ 99.0%) was used.

For cation analysis, test solutions were prepared from metal salts: mercury (II) acetate (Fluka, Munich, Germany, $\geq$98%), cadmium nitrate tetrahydrate (Fluka, Munich, Germany, $\geq$98%), copper acetate (II) monohydrate (Fluka, Munich, Germany, $\geq$98%), and lead (II) nitrate (Fluka, Munich, Germany, $\geq$99.5%). From the stock solutions of the mentioned metal salts (10^{-2} M), solutions with different concentrations were prepared by successive dilutions.

Electrochemical measurements were performed using a PGSTAT302N Autolab potentiostat connected to three-electrode cells. For **G** electrochemical characterization and preparation of CMEs, the *preparation cell* was used having a glassy carbon (GC) disc (Metrohm, Herisau, Switzerland) with a diameter of 3 mm (GC3) as the working electrode (WE), a platinum wire as the counter electrode (CE), and Ag/ 10 mM AgNO$_3$, 0.1 M TBAP/CH$_3$CN as the reference electrode (RE). After the experiments, the potentials were referred to as the potential of the ferrocene/ferrocenium (Fc/Fc$^+$) redox couple. Other three-electrode cells were used for the CMEs characterization: *transfer cell*, containing ferrocene solutions, and *analysis cell*, for electrochemical detection of HMs ions in aqueous test solutions. In these last two cells, the working electrodes were bare or modified with **G** films GC discs, and the auxiliary electrode was a platinum wire. The reference electrodes were Ag/10 mM AgNO$_3$, 0.1 M TBAP/CH$_3$CN and Ag/AgCl, 3 M KCl, respectively.

The electrochemical experiments for the characterization of **G** were performed under an argon atmosphere.

Cyclic voltammetry (CV), differential pulse voltammetry (DPV), and rotating disc electrode voltammetry (RDE) methods were used to characterize the electrochemical behavior of the ligand. The oxidation/reduction curves were initially recorded separately on the freshly cleaned GC3 electrode in 0.1 M TBAP, CH$_3$CN (support electrolyte), which was polarized starting from the stationary potential to positive/negative potentials. **G** was then added to the synthesis cell and these curves were recorded for **G** solutions of decreasing millimolar concentrations, according to DPV and RDE methods. In this paper, we noted the molar concentration of a reactant **G** with [**G**]. In CV, the curves were recorded at scan rates between 0.05 and 0.5 V/s. DPV curves were recorded at 0.01 V/s with a pulse height of 0.025 V and a time step of 0.2 s. RDE curves were obtained at 0.01 V/s with rotation rates between 500 and 1500 rpm.

The chemically modified electrodes based on **G** (**G**-CMEs) were prepared from millimolar solutions of **G** in 0.1 M TBAP/CH$_3$CN by scanning or controlled potential electrolysis (CPE). The GC electrode (3 mm diameter) inserted into the preparation cell containing the **G** solution was polarized at a defined potential that was maintained until a defined electric charge was reached. The resulting CME was removed from the preparation solution, blotted with fine paper, and rinsed with CH$_3$CN. CME was then introduced and conditioned (into the cell containing 0.1 M acetate buffer solution, pH = 4.5) by equilibration (15 CV cycles at 0.1 V/s between -0.89 V and 0.6 V) and overoxidation (15 CV cycles at 0.1 V/s between -0.19 V and 1.85 V). Then, the conditioned CME was introduced for 15 min into the mixture of HMs containing $5 \cdot 0^{-5}$ M of each cation (Cd^{2+}, Pb^{2+}, Cu^{2+}, and Hg^{2+}) in deionized water under controlled stirring. After that, the electrode was removed and placed in 0.1 M acetate buffer solution (pH = 4.5) and held for 3 min at -1 V, and then a DPV scan was initiated (0.01 V/s) from -1 V to 0.6 V. The resulting DPV curve was recorded and the current for each peak was measured relative to the baseline.

The results obtained by CV, DPV, and RDE, as standard techniques, are reliable due to the electrode shapes, preparation kits, and improved GC electrode cleaning procedure, and lead to reproducible surfaces before each experiment. However, additional errors may occur in electrode conditioning and subsequent analysis, leading to errors of around 10% for the analysis of HMs using CMEs obtained under the same preparation conditions.

All electrochemical experiments were conducted at 25 °C.

For the SEM analysis of the CMEs samples, a QUANTA Inspect F50 scanning electron microscope equipped with a field emission electron gun (FEG) with a resolution of 0.2 nm

and an X-ray energy dispersive spectrometer (EDS) with a resolution at MnK of 133 eV were used.

XPS analysis was conducted on a Thermo Scientific K-Alpha spectrometer operating with monochromatic Al Kα X-rays (1486.6 eV) at a 90° take-off angle. Survey and high-resolution spectra were recorded at 200 eV and 20 eV, respectively. For the deconvolution of core-level spectra, a mixed Gaussian–Lorentzian function was used after performing a Shirley background subtraction.

For surface examination by SEM and XPS, CME samples were prepared on glassy carbon (GC) discs with diameters of 8 mm, which have discs with a diameter of 6 mm (GC6) as the exposed surface, using amounts of electricity proportional to the exposed surface.

3. Results and Discussion

3.1. Chemically Modified Electrodes Preparation

New **G**-based modified electrodes were prepared by electropolymerization in millimolar solutions of **G** ligand in the supporting electrolyte (0.1 M TBAP/CH$_3$CN). Electrochemical immobilization of **G** on the GC electrode was performed either by sweeping the potential in the anodic range or by CPE at different anodic potentials and charges. Table 1 shows the different preparation conditions of **G**-CMEs formed by electrochemical oxidation, as well as the evidence of film formation brought by different methods: redox probe with ferrocene, chronoamperometry, SEM, XPS, and HM detection.

Table 1. Samples of modified electrodes prepared by scanning (S*) in 15 cycles between the given potentials (in V) or by CPE from **G** solutions.

CME's Number	[G] (mM)	CME's Preparation/GC Electrode	Electric Charge (mC)	CME's Characterization
1	1	S* (0–0.6)/GC3	-	Fc *a
2	1	S* (0–1.1)/GC3	-	Fc *a
3–3b	1	CPE at 0.6 V/GC3	1, 1.5	Chronoamperometry, Fc *a
4–4b	1	CPE at 0.6 V, 1.1 V/GC3	1	Chronoamperometry, Fc *a
5–5g	2	CPE at 0.6 V/GC3	1	Chronoamperometry, HMs *b
CME 6–6g	1	CPE at 0.6 V/GC3	1	Chronoamperometry, HMs *b
CME 7–7c	1	CPE at 0.6 V/GC3	0.5, 2, 5	Chronoamperometry, HMs *b
CME 8–8b	2	CPE at 1.1 V, 1.7 V/GC3	1	Chronoamperometry, HMs *b
CME 9	1	S* (0–2.5)/GC6	-	SEM
CME 10	1	CPE at 0.6 V/GC6	2	Chronoamperometry, SEM, XPS
CME 11	1	CPE at 0.6 V/GC6	4	Chronoamperometry, SEM, XPS, Nano-FTIR
CME 12	1	CPE at 0.6 V/GC6	8	Chronoamperometry, SEM, XPS
CME 13	1	CPE at 1.1 V/GC6	2	Chronoamperometry, SEM, XPS
CME 14	1	CPE at 1.1 V/GC6	4	Chronoamperometry, SEM, XPS
CME 15	1	CPE at 1.1 V/GC6	8	Chronoamperometry, SEM, XPS
CME 16	1	CPE at 1.1 V/GC6	20	Chronoamperometry, SEM, XPS
CME 17	1	CPE at 2.5 V/GC6	20	Chronoamperometry, SEM, XPS

*a Transfer of CME in Fc solution in 0.1 M TBAP/CH$_3$CN; *b HMs detection.

3.2. Evidence for Film Formation through Ferrocene Redox Probe

Figure 2 shows the CV curves corresponding to obtaining **G**-CME through 15 successive cycles with the anodic limit of 0.6 V and 1.1 V, respectively (Figure 2a), as well as those obtained after transferring these modified electrodes into the Fc solution (Figure 2b). The

dotted line represents the curves obtained for Fc on the bare electrode. In the lower part of Figure 2, the chronoamperograms corresponding to obtaining **G**-CME through CPE are represented (Figure 2c), as well as the CV curves resulting from the transfer of electrodes modified through CPE into the Fc solution (Figure 2d), in relation to the obtained Fc signal on the bare electrode with a film represented by a dotted line. Table 2 shows the main signal characteristics for Fc obtained from the CV curves: anodic peak potential (Epa) and cathodic peak potential (Epc) for the Fc/Fc$^+$ couple, the difference between Epa and Epc (ΔEp), and the formal potential (Ef) of the couple Fc/Fc$^+$ for each **G**- CME.
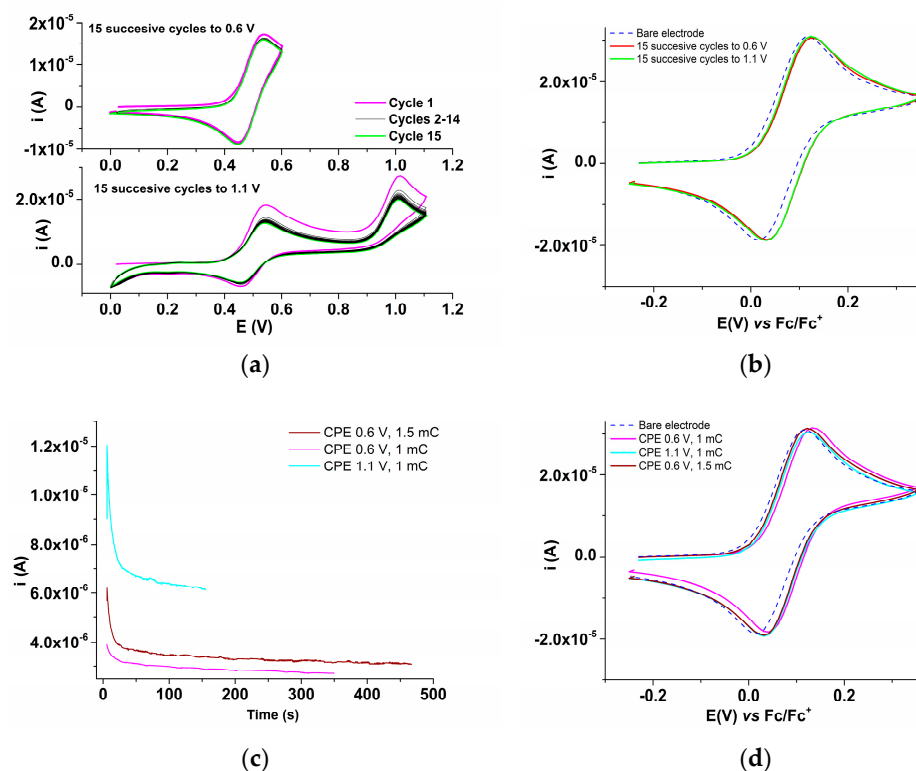
Figure 2. Successive CVs (0.1 V/s, 15 cycles) in a solution of **G** (1 mM) in 0.1 M TBAP/ CH$_3$CN performed at two anodic potential thresholds (0.6 V and 1.1 V) (**a**); CV curves (0.1 V/s) after transfer of **G**-CMEs obtained by sweeping in ferrocene solution in 0.1 M TBAP/CH$_3$CN—solid lines vs. bare electrode—dashed line (**b**); chronoamperograms during the preparation of **G**-CMEs by CPE at different potentials and charges (**c**); CV curves (0.1 V/s) after transfer of **G**-CMEs obtained by CPE in ferrocene solution in 0.1 M TBAP/CH$_3$CN, solid lines, vs. bare electrode, dashed line (**d**).

Table 2. Potentials of ferrocene anodic (Epa) and cathodic (Epc) peaks in ferrocene solution in 0.1 M TBAP/CH$_3$CN on a bare electrode and on the **G**-CMEs prepared by scanning and CPE for different conditions of preparations in solution with [**G**] = 1 mM.

Crt. Nr.	Method of Preparation and Conditions	Epa (V)	$10^5 \cdot$ ipa (A)	Epc (V)	$10^5 \cdot$ ipc (A)	ΔEp [*1] (mV)	Ef [*2] (V)
1	Bare electrode	0.121	3.161	0.020	−1.888	101	0.071
2	15 successive cycles at 0.6 V	0.124	3.090	0.032	−1.878	92	0.080
3	15 successive cycles at 1.1 V	0.122	3.117	0.033	−1.878	89	0.078
4	CPE 0.6 V, 1 mC	0.134	3.169	0.042	−1.836	92	0.088
5	CPE 1.1 V, 1 mC	0.125	3.039	0.035	−1.914	90	0.080
6	CPE 0.6 V, 1.5 mC	0.123	3.146	0.033	−1.922	90	0.078

[*1] ΔEp = Epa − Epc; [*2] Ef = (Epa + Epc)/2.

From Figure 2 and Table 2, it can be seen that the main characteristics of Fc in the CV curves are slightly different for the modified electrode in relation to the electrode not covered with a film. The anodic peak potential (Epa) is higher, as was expected after coating the electrode with a film. The cathodic peak potential (Epc) is also higher (and varies more than Epa), and the difference between Epa and Epc (ΔEp) is smaller than on the bare electrode, suggesting the formation of thin films on the surface. The formal potentials (Ef) of ferrocene on **G**-CME are higher than those measured on the bare electrode, which confirms the coating of the electrode with films. Comparison of the results for ΔEp and Ef in lines 2 and 3 in Table 2 shows that film formation is not favored by cycling up to 1.1 V over a potential of 0.6 V, which also follows from the comparison of lines 4 and 5 in which the film formation is by CPE at potentials of 0.6 V and 1.1 V, respectively. This means that regardless of the film formation method, increasing the potential does not favor film formation. Comparing the values of ΔEp and Ef in rows 4 and 6 of Table 2, it can also be seen that an increase in the amount of electricity does not lead to an increase in ΔEp or Ef. And this fact confirms the formation of thin films.

The influence of the main parameters that can be optimized during film formation (electropolymerization potential and electric charge) on the properties of the films obtained under different conditions was analyzed. Regardless of the film formation method, increasing the potential does not favor **G**-based film formation. It has been observed that an increase in the amount of electric charge used in film preparation does not lead to features specific to thicker films. This behavior could be rationalized by analyzing the electropolymerization reaction from a kinetic point of view. From Figure 2c, it can be seen that the application time of the 1.1 V potential step is shorter (approx. 180 s) than for the 0.6 V step (approx. 360 s) to achieve the same amount of electricity. From a kinetic point of view, it follows that the reaction time for polymerization is reduced. Consequently, the formation of the polymer is not favored in the sweep with the anodic limit of 1.1 V compared to the one up to 0.6 V.

3.3. Characterization of Chemically Modified Electrodes by SEM

G-CMEs prepared under different conditions were examined by SEM at different magnifications. Their images indicate that the deposits are continuous and nanostructured, with formations ranging in size from 5 to 100 nm (Figures 3, 4 and S1–S9).
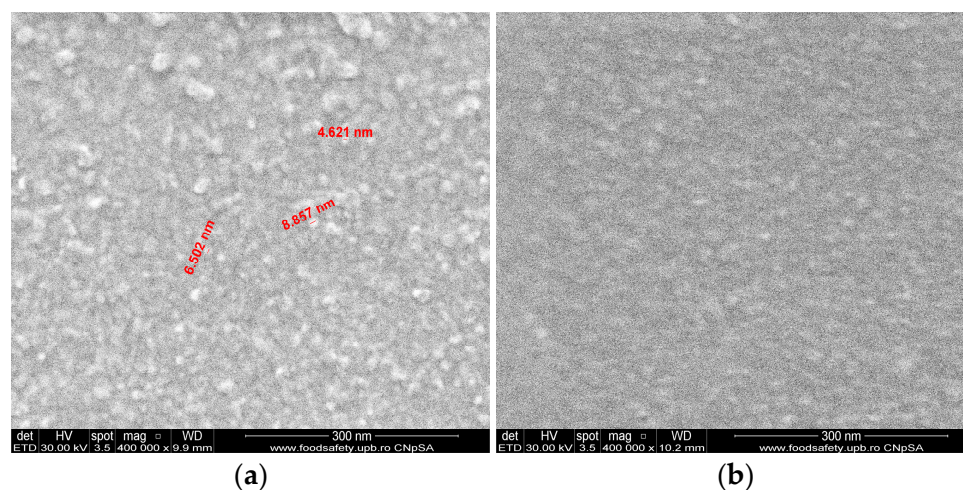

Figure 3. SEM images at magnifications of 400,000 for CMEs obtained by scanning (**a**) and CME by CPE (**b**) corresponding to CME 9 (scanning) and CME 11 (CPE at 0.6 V, 4 mC), respectively.
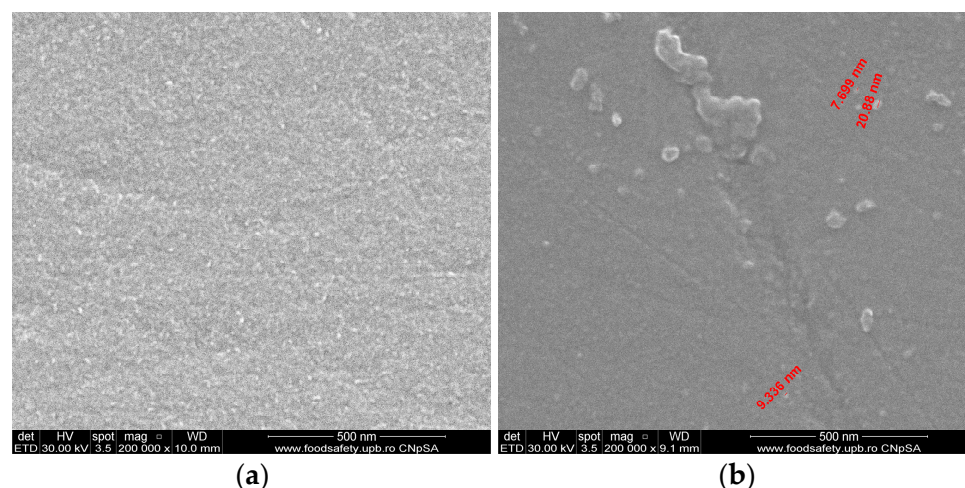
Figure 4. SEM images at magnifications of 200,000 for CMEs obtained by CPE at 0.6 V (**a**) and 1.1 V (**b**) corresponding to CME 12 (CPE at 0.6 V, 8 mC) and CME 15 (CPE at 1.1 V, 8 mC), respectively.

Figure 3 shows SEM images for CMEs obtained by scanning (a) and by CPE (b) corresponding to CME 9 and CME 11, respectively (Table 1). It can be seen that the CMEs prepared by scanning (Figure 3a) are structured differently from those obtained by CPE (Figure 3b), having formations between 4.6 and 8.9 nm for those prepared by scanning and 5.9–6.7 nm for those prepared by CPE. CMEs prepared by scanning appear less uniform than those prepared by CPE. From the analysis of the films obtained by CPE, it turns out that the uniformity is closely related to the electric potential and charge used in the preparation of the modified electrode (Figures 3 and 4). When we compare Figures 3b and 4a for CMEs obtained at the same potential (0.6 V) and with different charges, it turns out that those obtained using higher charges are smoother. When we compare Figure 4a,b for CMEs obtained at the same electric charge (8 mC) and at different potentials, we notice that the films obtained at the potential of 0.6 V are more uniform than those obtained at 1.1 V.

Comparisons were made between the surface images for CMEs prepared by CPE at different potentials. Analyzing the images obtained (at the same electric charge of 2 mC and different potentials), it can be seen that the films from the potential of 0.6 V (Figure S2) are structured differently compared to the films obtained at 1.1 V (Figure S5), with the films from 0.6 V being more uniform. The same remark can be made for the films prepared with 4 mC at 0.6 V (Figure S3) and 1.1 V (Figure S6), with the films prepared at 0.6 V appearing more uniform than those prepared at 1.1 V. Comparing Figures S8 and S9 obtained for the films of 20 mC, prepared at 1.1 V and 2.5 V, respectively, it follows that for the film prepared at a higher potential exhibits a more uniform coverage.

For the films prepared at 0.6 V (Figures S2–S4) with electropolymerization charges increasing from 2 to 8 mC, the appearance of the deposition is more uniform for the films prepared at bigger charges. Thus, the films prepared at 8 mC show formations of about 6 nm, while the films prepared at 2 mC show formations of about 20 nm. With the increase of the electric charge at the potential of 0.6 V, the uniformity of the deposited film increases.
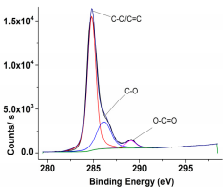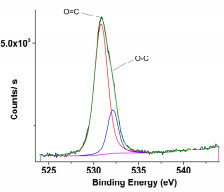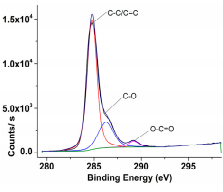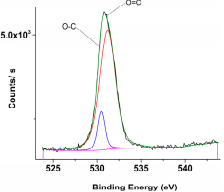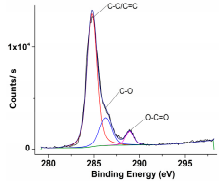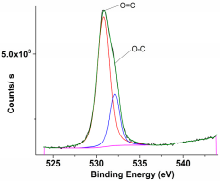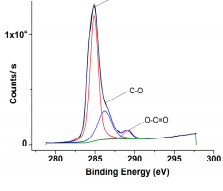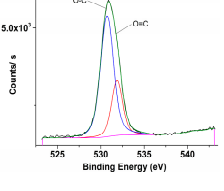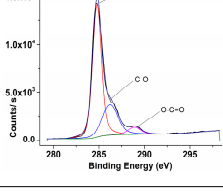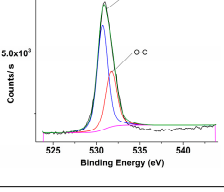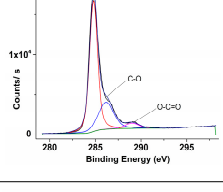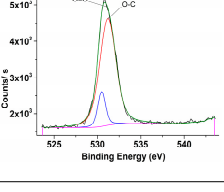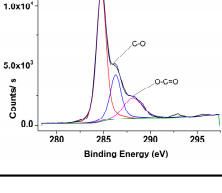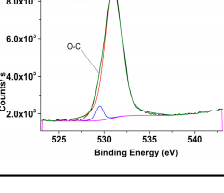
For the films prepared at 1.1 V (Figures S5–S8) with electropolymerization charges increasing from 2 to 20 mC, the appearance of the deposition is less uniform in the films prepared at bigger charges. Thus, the films prepared at 8 mC show agglomerates of about 20 nm, while the films prepared at 2 mC show formations of about 5 nm. With the increase of the electric charge at the potential of 1.1 V, the uniformity of the deposited film decreases.

The uniformity of the deposited film depends most on the potential. The increase of the electric charge in CPE does not affect the film smoothness obtained at different potentials in the same way.

3.4. Characterization of Chemically Modified Electrodes by XPS

XPS analysis results for C 1s and O 1s core-level spectra of **G**-CMEs are collected in Table 3. The preparation conditions (column 2 of Table 3) refer to the preparation potential and the amount of electric charge used.

Table 3. C 1s and the O 1s XPS core-level spectra of the polymer surfaces obtained on GC6 by CPE in different conditions of preparation.

Modified Electrode	Conditions for CPE	C 1s	O 1s
CME 10	0.6 V; 2 mC ($28\ mC/cm^2$)		
CME 11	0.6 V; 4 mC ($56\ mC/cm^2$)		
CME 12	0.6 V; 8 mC ($112\ mC/cm^2$)		
CME 13	1.1 V; 2 mC ($28\ mC/cm^2$)		
CME 14	1.1 V; 4 mC ($56\ mC/cm^2$)		
CME 16	1.1 V; 20 mC ($280\ mC/cm^2$)		
CME 17	2.5 V; 20 mC ($280\ mC/cm^2$)		

The amount of electric charge used was expressed either as the charge (in mC) or as the charge per surface unit (in mC/ cm^2) for GC6 (used for examination of surfaces). The charge density was kept the same for all types of analyses in order to correlate the information related to the surface structure with those resulting from the analysis of HMs.

The chemical structure at the surface of **G**-CMEs analyzed by XPS allows visualization of C 1s spectra deconvoluted into three peaks [26]. According to the figures entered in Table 4, the peak at around 284.8 eV was assigned to the C–/C=C bonds and originates from azulene conjugated honeycomb network. The peak at around 286.2 eV was assigned to C–O, and the peak at around 289 eV corresponds to the O–C=O bond. The latter two peaks originate from the oxazolone film deposited on the GC electrode. The spectra at C 1s core level (Table 3) allowed a closer inspection of the chemical state of the obtained polymer, as summarized in Table 4. Furthermore, to better understand how the variation of the two parameters (the amount of electricity and applied potential) during electropolymerization affects the structure of the electrode surface, the ratio of C–C/C–O and C–C/O–C=O was calculated.

Table 4. Data for high-resolution C 1s XPS core-level spectra for **G** films obtained by electropolymerization at different conditions: binding energy (BE), assignment, atomic percentage (At%), normal area (area (N)), and C–C/C–O and C–C/O–C=O ratios.

Nr. Crt	Sample (E; q)	BE	Assignment	At%	Area (N)	C–C/C–O	C–C/O–C=O	C/O (%)
1	CME 10 (0.6 V; 28 mC/cm^2)	284.81 286.12 289.03	C–C/C=C C–O O–C=O	71.20 23.81 4.99	284.92 95.28 19.99	2.99	14.25	7.14
2	CME 11 (0.6 V; 56 mC/cm^2)	284.79 286.26 289.20	C–C/C=C C–O O–C=O	73.94 22.68 3.38	293.8 90.12 13.43	3.26	21.87	7.44
3	CME 12 (0.6 V; 112 mC/cm^2)	284.79 286.27 288.91	C–C/C=C C–O O–C=O	74.81 18.96 6.24	280.36 71.05 23.37	3.95	11.99	5.06
4	CME 13 (1.1 V; 28 mC/cm^2)	284.88 286.20 289.08	C–C/C=C C–O O–C=O	60.84 22.90 3.63	16,096.32 6055.36 959.13	2.66	16.78	6.10
5	CME 14 (1.1 V; 56 mC/cm^2)	284.79 286.21 288.89	C–C/C=C C–O O–C=O	67.86 27.06 5.08	258.75 103.18 19.37	2.51	13.36	5.44
6	CME 16 (1.1 V; 280 mC/cm^2)	284.80 286.16 289.00	C–C/C=C C–O O–C=O	68.65 26.73 4.62	279.11 108.67 18.79	2.57	14.85	8.93
7	CME 17 (2.5 V; 280 mC/cm^2)	284.78 286.29 288.12	C–C/C=C C–O O–C=O	60.18 22.70 17.12	220.74 83.27 62.79	2.65	3.52	3.62

From the data reported in Table 4, the following effects can be observed: when the electric charge increases (lines 1, 2, 3), the C–C/C–O ratio increases with the electric charge (from 2.99 in the case of the CME 10 sample to about 3.95 in the case of sample CME 12—the potential being constant at 0.6 V). This result is different from that obtained for CMEs based on a similar azulene structure substituted with 4,6,8-trimethyl groups (**M**-CMEs) [1]. Comparing lines 1 and 4, when the potential increases from 0.6 V (CME 10) to 1.1 V (CME 13), this ratio decreases from 2.99 to 2.66. Similarly (lines 2 and 5), when the potential increases from 0.6 V (CME 11) to 1.1 V (CME 14), the ratio decreases from 3.26 to 2.51, but when the potential increases from 1.1 V (CME 16) to 2.5 V (CME 17), this ratio varies slightly from 2.58 to 2.65 (lines 6 and 7).

Based on the data presented in Table 4, it can be stated that the variation of the electropolymerization potential from +0.6 V to +1.1 V leads to significant changes in the polymer surface. This observation is in agreement with the SEM results (Figure 4).

From the survey curves, the atomic ratio between the percentage of C and O (C/O) was calculated (Table 4, column 9), which indicates decreases with the increase of the potential applied in the CPE. The calculated values for the C/O ratio are in agreement with the intensification of the polymer oxidation upon increasing the potential applied to the preparation of **G**-CMEs.

3.5. Characterization of Chemically Modified Electrodes by Nano-FTIR

Scattering-type scanning near-field optical microscopy (s-SNOM) is a scanning probe method used in optical microscopy and spectroscopy that surpasses the typical light diffraction limit, achieving under 10-nanometer spatial resolution. It relies on tightly confining light at the tip of a metallic AFM probe to create a nanoscale optical hotspot. By analyzing the scattered light, it extracts optical properties and generates nanoscale images alongside mechanical data. This technology has evolved to enable hyperspectral, nanoscale Fourier transform spectroscopy (Nano-FTIR) using broadband radiation [27,28]. With tunable IR light sources, s-SNOM systems enabled nanoscale chemical mapping in 30–300 s per image.

Material-selective mid-IR frequencies were used to comprehensively characterize some of the obtained CMEs (Figure 5). s-SNOM imaging led to characteristic material maps of the chemical and optical properties of the sample surface simultaneously with topography imaging (AFM). Nano-FTIR spectra were recorded on the rough surface (Figure 5a) which, by averaging (at different points of the deposited material), led to the spectrum represented by the blue line (from Figure 5d) that indicates the presence of the polymer.
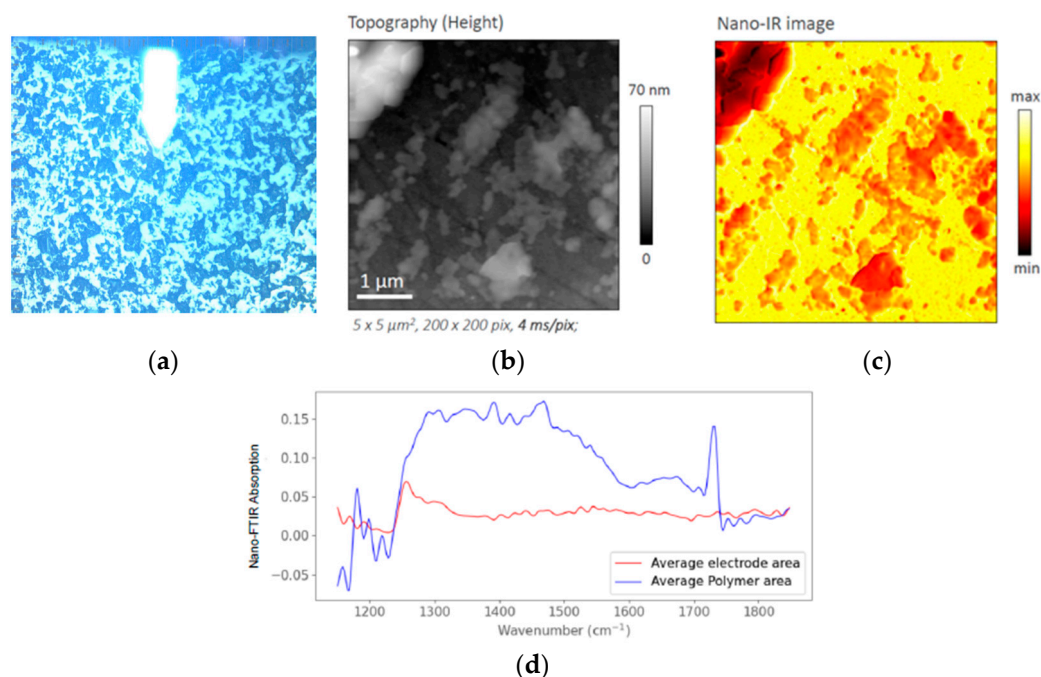

(**a**)　　　　　　　　　(**b**)　　　　　　　　　(**c**)

(**d**)

Figure 5. AFM image (**a**), topographic (AFM) image (**b**), characteristic material map (**c**), and nano-FTIR spectra on the bare and film-coated electrode (**d**) surface of CME 11.

The nano-FTIR spectra measured on the smooth area not covered with the film are devoid of lines for specific absorptions (red line in Figure 5d). The nano-FTIR spectra of the polymer show characteristic absorption bands around 1730, 1393, and 1287 cm^{-1}. Research is ongoing.

3.6. HMs Recognition Experiments Using Chemically Modified Electrodes

CMEs obtained by the CPE method were used for the analysis of HMs ions. This method provides good reproducibility due to rigorous control of potential and charge during electropolymerization. After preparation, equilibration, and superoxidation, **G**-CMEs were introduced into synthetic HMs samples prepared in deionized water (containing HMs ions in equal concentrations), and the anodic stripping procedures established in our laboratory followed. After the polarization at -1 V, in which the cations in the polymer film were reduced to metallic species, a potential scan was initiated. The obtained DPV curve shows distinct stripping peaks for each of the studied ions: Cd(II), Pb(II), Cu(II), and Hg(II). The various values of the stripping potentials demonstrate that these ions were complexed differently in the electrogenerated films. For example, on CMEs obtained at 0.6 V and 1 mC, DPV redissolution peaks of these ions were observed at the following potentials: -0.84 V, -0.59 V, -0.13 V, and 0.22 V, for Cd(II), Pb(II), Cu(II), and Hg(II), respectively. The presence of a peak of -0.59 V indicates that the analyzed sample contained Pb(II). The concentration of Pb(II) in the sample can be obtained from the calibration curve.

These DPV potentials vary slightly with the concentration of metal ions in the analyzed mixture. These values are more negative than those obtained using **M**-modified CMEs [1], whose values are located at -0.80, -0.54, -0.08, and 0.23 V.

The peaks obtained for the analyzed ions have different intensities. This demonstrates that these ions were complexed differently in the electrogenerated films. The stripping peak for lead ions is the highest.

The influence of the film-forming potential and electric charge used in the CPE on the DPV response was examined for each of the HM cations that were tested.

Figure 6 shows the influence of the film formation potential for CMEs prepared by CPE at different potentials (0.6 V, 1.1 V, 1.7 V, and 2.5 V) but using the same electric charge (2 mC). Figure 6a shows that the chronoamperograms obtained during the preparation of CMEs present currents with very different intensities and different times of application of the potential step, which indicates that the state of the prepared surface varies greatly when different potentials are used. Figure 6b shows the DPV curves for CMEs prepared at different potentials. Figure 6c indicates an increase in peak current for each cation with increasing preparation potential.
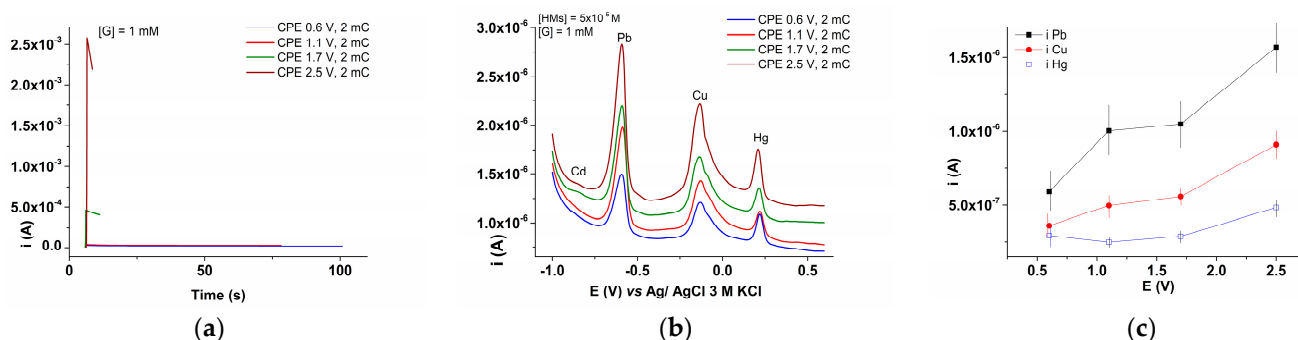

Figure 6. Chronoamperograms for the preparation of CMEs by CPE using the same 2 mC charge from solutions with [**G**] = 1 mM at different potentials: 0.6 V (blue), 1.1 V (red), 1.7 V (green), and 2.5 V (wine) (**a**); DPV curves after the complexation step with HMs (from the solution containing equal concentrations (of $5 \cdot 10^{-5}$ M each) of Cd(II), Pb(II), Cu(II), and Hg(II) using the CMEs prepared by CPE at different potentials: 0.6 V (blue), 1.1 V (red), 1.7 V (green), and 2.5 V (wine) (**b**); dependence of the peak currents for each HM cation on the applied potential in the CPE (**c**).

From Figure 6c it is noticed that for the same concentration of analyzed HMs, the highest values for peak currents are obtained for Pb, followed by Cu (values approximately 2 times lower than for Pb) and Hg (values approximately 2 times lower than for Cu). The peak currents for Cd are very small. The result is that the Pb ion is preferentially complexed by the film of **G**-CMEs.

Figure 7 shows the influence of the electric charge on the chronoamperograms (Figure 7a), the DPV curves (Figure 7b), and the peak currents (Figure 7c) for the analyzed ions. It follows from this figure that an increase in the electric charge does not lead to a major improvement in the analytical signal (peak current) for the analyzed ions. For the detection of HMs using chemically modified electrodes starting from this guayazulenyloxazolone, the preparation conditions of **G**-CMEs should be further optimized.

(**a**)   (**b**)   (**c**)
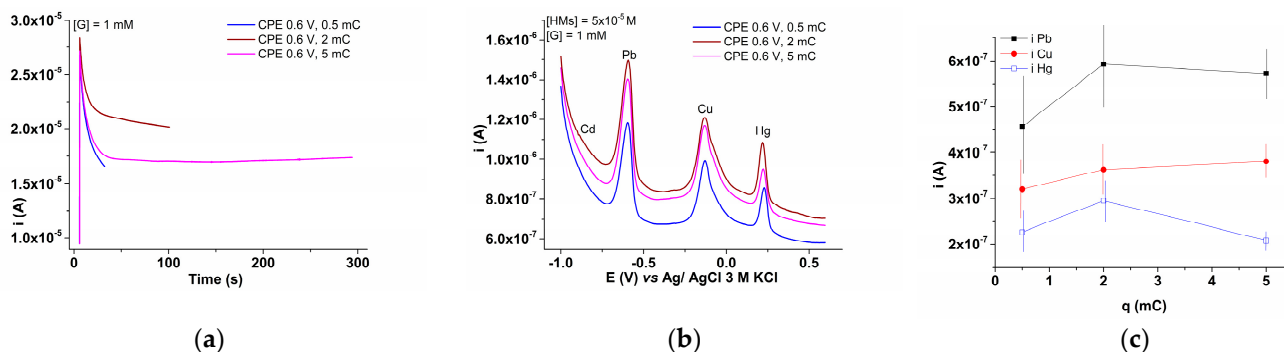
Figure 7. Chronoamperograms for the preparation of CMEs by CPE at 0.6 V from solutions with [**G**] = 1 mM using electric charge amounts of 0.5 mC (blue), 2 mC (wine), and 5 mC (magenta) (**a**); DPV curves after the complexation step with HMs (from a solution containing equal concentrations of Cd(II), Pb(II), Cu(II), and Hg(II)—$5 \cdot 10^{-5}$ M each) using the prepared CMEs by CPE as in Figure 7a (**b**); dependence of the peak currents on the amount of electric charge used to prepare the films (**c**).

G-CMEs were used to draw the calibration curves for HM analysis (Figure 8). For accumulation, test solutions with equal concentrations of HMs between 10^{-7} M and 10^{-4} M were used. Among the investigated ions, the best results were obtained for Pb ions. The obtained curves indicate a saturation of the film for all analyzed ions.
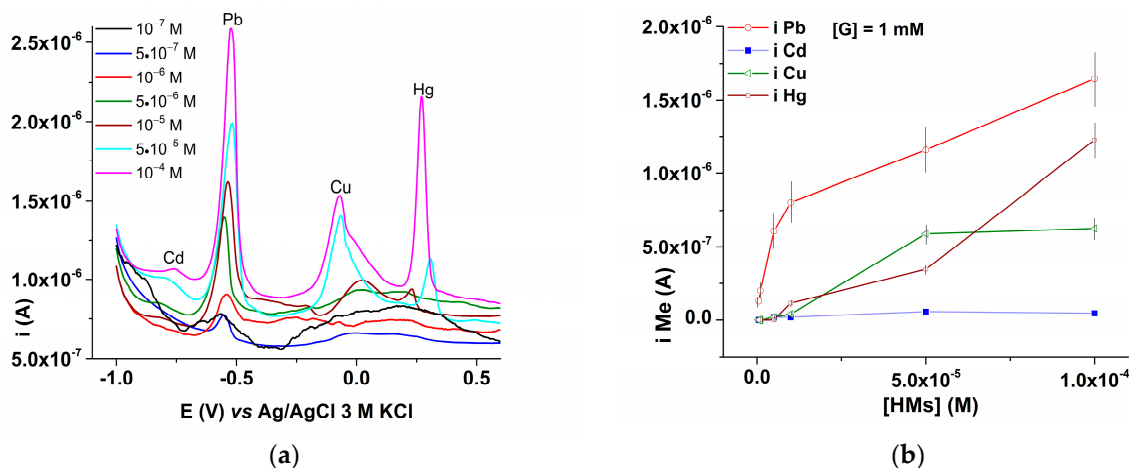

(**a**)   (**b**)

Figure 8. DPV (0.01 V/s^{-1}) curves recorded on **G**-CMEs (obtained by CPE at 0.6 V and 1 mC in [**G**] = 1 mM) (**a**); calibration curves for HMs ions on CMEs resulting from Figure 8a (**b**).

Linear dependences of the peak currents for Pb on the concentration of these ions ([Pb]) were obtained for the concentration range between 10^{-7} M and $5 \cdot 10^{-5}$ M. For **G**-CMEs prepared at 0.6 V using 1 mC films, detection limits for each HM ion were estimated from the dependences of DPV peak currents on metal ion concentrations: [Cd(II)] = $5 \cdot 10^{-6}$ M; [Pb(II)] = 10^{-7} M; [Cu(II)] = $5 \cdot 10^{-6}$ M; and [Hg(II)] = 10^{-5} M.

3.7. Electrochemical Characterization of the Ligand

CV, DPV, and RDE methods were used to characterize the electrochemical behavior of the ligand in acetonitrile solutions. The oxidation and reduction curves in the supporting

electrolyte were initially recorded. These curves recorded in the absence of ligand at the beginning of each experiment were represented by dashed lines. These curves were then recorded for **G** solutions of different concentrations. The peaks observed on these curves were noted in the order in which they appear on the voltammograms obtained by DPV, which were taken as a reference for scoring for the other methods. For better comparison of current values, cathodic currents were sometimes represented in their absolute values.

3.7.1. Ligand Characterization by CV and DPV

The characterization of **G** by CV and DPV is summarized in Figure 9, where the obtained curves are presented in parallel to compare the two methods. Four anodic peaks (a1–a4) and five cathodic peaks (c1–c5) were highlighted. The oxidation (a1–a4) and reduction (c1–c5) processes highlighted by the electrochemical studies of the **G** ligand intensify linearly with increasing **G** concentration. The peak potentials are properly correlated in CV and DPV (the peak potential in DPV is located at a potential close to the semi-peak potential in CV).
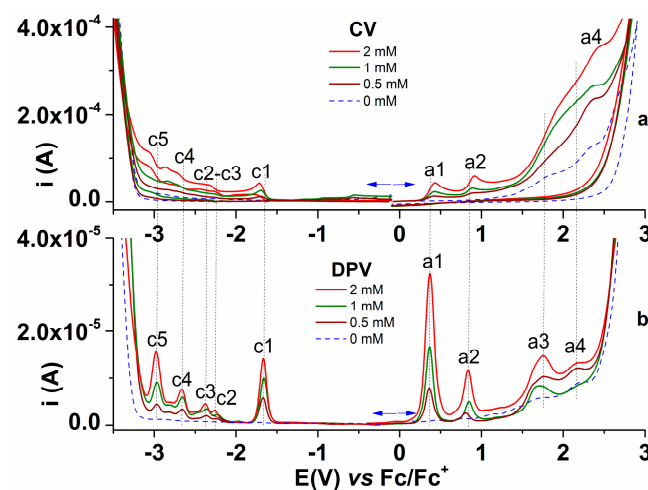
Figure 9. CV (**a**) and DPV (**b**) curves for different concentrations of **G** in 0.1 M TBAP/ CH$_3$CN; all cathodic currents are shown in absolute values.

The CV curves at different scan rates in the domains of the first oxidation process a1 and first reduction process c1 are reproduced in Figure 10. The peak a1 is reversible. It presents a peak a1′ in the return scan, and has a current that varies with the square root of the scan rate with a slope close in absolute value to that of a1 peak ($7 \cdot 10^{-6}$ A·V$^{-1/2}$ · s$^{1/2}$). The first reduction process c1 is less reversible than a1, and was considered quasi-reversible. In the return scan, c1 shows c1′ the corresponding peak that has a lower slope in absolute value than that for c1 (Figure 10b).
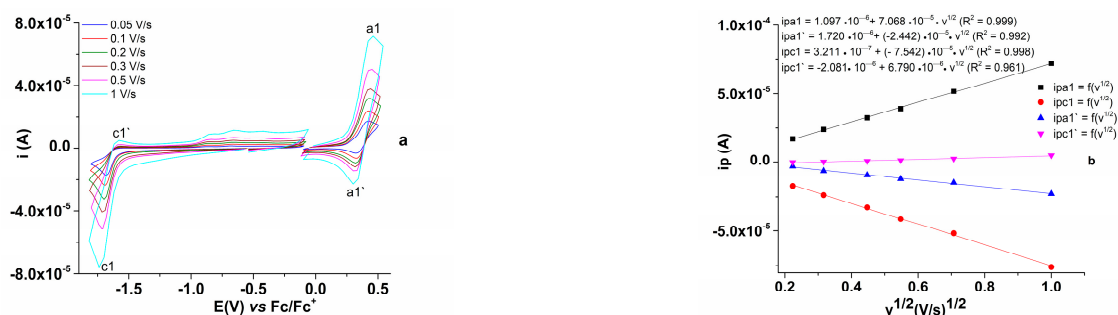

Figure 10. CV curves in anodic and cathodic scans at different scan rates for [**G**] = 1 mM in 0.1 M TBAP, CH$_3$CN (**a**); linear dependences of the peak currents for (a1) and (c1), respectively, vs. the square root of the scan rate (**b**).

The linear dependences of the peak currents in CV for (a1) and (c1), respectively, against the square root of the scan rate have symmetrical currents, with similar slopes. This indicates that the first electron transfer has a similar degree of reversibility in the anodic and cathodic processes. However, the corresponding a1 and c1 peaks in the anodic and cathodic DPV curves are less balanced, with the current of a1 being almost double that of c1. Therefore, the first oxidation process is more intense than the first reduction process. This behavior could be the result of a larger number of electrons involved in the first oxidation than in the first reduction. A comparison between the electrochemical behavior of several azulenic ligands that are correlated with the structures of the ligands will allow the development of a mechanism to justify the number of electrons involved in the first oxidation and reduction processes.

The curves obtained in Figure 11 over different scan domains also show a more pronounced reversibility of peak a1 relative to c1, which is in agreement with the assessment of peaks a1 as reversible and c1 as quasi-reversible based on the shape of CV curves (Table 5).
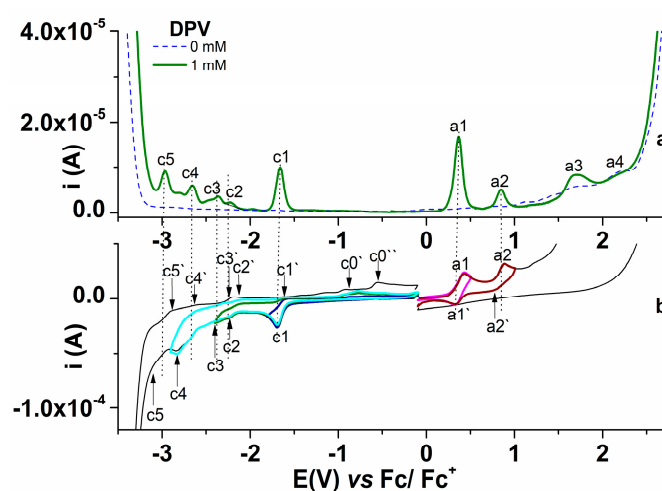

Figure 11. Curves for **G** in TBAP/CH$_3$CN 0.1 M at 1 mM concentration obtained by DPV (**a**) and CV (0.1 V/s) on different anodic and cathodic scan domains (**b**); all cathodic currents in the DPV are shown in absolute values.

Table 5 shows the values of the peak potentials resulting from the CV and DPV curves and the half-wave potentials (E$_{1/2}$) resulting from the RDE curves together with the characteristics related to the reversibility of the highlighted processes.

3.7.2. Ligand Characterization by RDE

Figure 12 illustrates in parallel the RDE and DPV curves obtained for **G** stationary electrode GC3. The RDE curves were obtained at different rotation rates of the rotating disc electrode (Figure 12b), as well as at different concentrations of **G** for the same rotation rate (Figure 12c).

Table 5 shows the values of the peak potentials resulting from the CV and DPV curves and the half-wave (E$_{1/2}$) resulting from the RDE curves.

Based on the CV, DPV, and RDE curves (Figures 9–12), the main electrochemical transformation processes of the **G** ligand that were differently highlighted by these voltammetric methods were identified (Table 5). Phenyl-oxazolone **G** shows electrochemical characteristics different from those identified for phenyl-oxazolone **M** [1], especially for the first two oxidation processes: process a1 is reversible for **G,** while for **M** it is quasi-reversible; process a2 is quasi-reversible for **G** and irreversible for **M**. This fact can have important consequences related to the polymerization of these structures. The RDE curves for **G** show that processes a1 and a2 have a behavior of regular waves with limiting currents that increase linearly with the concentration of **G**, while for **M,** anodic RDE curves are very close to the background current. These matters are under investigation.

Table 5. Values (in V) for the peak potentials in the CV and DPV curves and for the half-wave potentials ($E_{1/2}$) for the waves in the RDE curves and the characteristics of the electrochemical processes undergone by **G** in 0.1 M TBAP/CH$_3$CN solutions resulting from the sweeps towards anodic (a) and cathodic (c) potentials.

Peak (G)	Method			Peak Characteristics
	CV	**DPV**	**RDE ($E_{1/2}$)**	
a1	0.444	0.375	0.366 (0.5 mM) 0.373 (1 mM) 0.380 (2 mM)	Reversible
a2	0.912	0.837	0.870 (0.5 mM) 0.888 (1 mM) 0.916 (2 mM)	Quasireversible
a3	-	1.756	1.624 (0.5 mM) 1.595 (1 mM) 1.456 (2 mM)	Irreversible
a4	2.481	2.188	-	Irreversible
c1	−1.703	−1.664	−1.664 (0.5 mM) −1.663 (1 mM) −1.671 (2 mM)	Quasireversible
c2	−2.318	−2.258	−2.266 (0.5 mM) −2.293 (1 mM) −2.339 (2 mM)	Quasireversible
c3	−2.850	−2.378	-	Quasireversible
c4	-	−2.662	-	Quasireversible
c5	−3.080	−2.974	-	Quasireversible
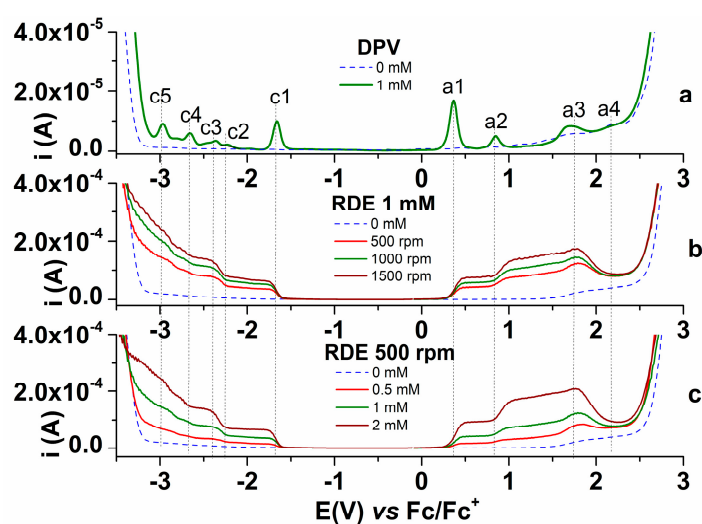
Figure 12. DPV curve (**a**) and RDE curves (**b**,**c**) on GC recorded in solution of **G** in 0.1 M TBAP/CH$_3$CN; in (**a**,**b**) [**G**] = 1 mM; RDE curves at 500 rpm (**c**) are recorded at different concentrations of **G** in 0.1 M TBAP/CH$_3$CN; cathodic currents in are shown in absolute values.

The RDE curves for processes a1 and a2 have a regular wave behavior with limiting currents that increase linearly with the **G** concentration. The appearance of the RDE curves in the anodic and cathodic range is different from that recorded for the similar ligand **M**, which shows that the intensities of the anodic and cathodic processes for the two ligands are different. It follows that the oxidation reactions occurring in the case of **G** lead to different characteristics of the film than in the case of **M**. The two structures of the **M** and **G** ligands are practically identical in terms of electron density, and the differences

created by the alkyl groups are not of major importance in the distribution of charge in the positions to be considered. The active position in the case of oxidation (polymerization) is position three, which leads to obtaining a stable tropylium ion on the seven-atom ring. This position is vacant in **M**, and in the case of polymerization, the proton can be removed after oxidation. In the case of **G**, position three is not free, and the methyl at this position creates problems, including that it can partially stabilize a positive charge at carbon three on the azulene. All these differences can be the cause of the formation of different films by electropolymerization of structurally close ligands. The study of the polymerization mechanism is ongoing.

4. Conclusions

This study summarizes electrochemical, SEM, and XPS experiments on chemically modified electrodes prepared by electropolymerization of 4-((5-isopropyl-3,8-dimethylazulen-1-yl)methylene)-2-phenyloxazol-5(4H)-one (**G**). The electrochemical study of the ligand by CV, DPV, and RDE allowed the identification of the potential values at which **G** undergoes electrochemical transformations through oxidation or reduction in the organic electrolyte, as well as the appreciation of their degree of reversibility. The results obtained by the three methods were concordant and complementary and led to the conclusion that thin films are obtained through oxidation, as in the case of a similar, differently substituted azulenic ligand.

Novel chemically modified electrodes based on **G** (**G**-CMEs) were obtained by potential scanning or controlled potential electrolysis (CPE) in anodic domains on glassy carbon electrodes. This study on the influence of the electropolymerization potential and the electric charge highlighted the formation of thin films. The surface properties of the films analyzed by SEM and XPS were concordant: the increase in the electropolymerization potential led to significant changes in the polymer surface and to a decrease of the atomic ratio between C and O. Testing **G**-CMEs obtained under different conditions for the analysis of HMs ions from aqueous solutions showed that increasing the applied potential used in the preparation of **G**-CMEs leads to improved analytical results, especially for Pb(II) ion.

Author Contributions: Conceptualization, E.-M.U.; methodology, E.-M.U.; software, R.T., A.M.P. and O.-T.M.; validation, E.-M.U.; formal analysis, A.-G.B., O.-T.M. and C.M.; investigation, A.-G.B., C.M., O.-T.M., A.M.P. and R.T.; resources; data curation, A.M.P. and E.-M.U.; writing—original draft preparation, A.-G.B.; writing—review and editing, E.-M.U., A.-G.B. and R.T.; visualization, E.-M.U., A.M.P. and R.T.; supervision, E.-M.U., A.M.P. and R.T.; project administration, E.-M.U. All authors have read and agreed to the published version of the manuscript.

References

1. Brotea, A.-G.; Matica, O.-T.; Musina (Borsaru), C.; Cristea, M.; Stefaniu, A.; Pandele, A.-M.; Ungureanu, E.-M. Advanced Materials Based on Azulenyl-Phenyloxazolone. *Symmetry* **2023**, *15*, 540. [CrossRef]

2. Vasile (Corbei), A.-A.; Ungureanu, E.-M.; Stanciu, G.; Cristea, M.; Stefaniu, A. Evaluation of(Z)-5-(Azulen-1-ylmethylene)-2-thioxothiazolidin-4-ones Properties Using Quantum Mechanical Calculations. *Symmetry* **2021**, *13*, 1462. [CrossRef]

3. Garcia-Sanz, C.; Andreu, A.; de las Rivas, B.; Jimenez, A.I.; Pop, A.; Silvestru, C.; Palomo, J.M. Pd-Oxazolone complexes conjugated to an engineered enzyme: Improving fluorescence and catalytic properties. *Org. Biomol. Chem.* **2021**, *19*, 2773–2783. [CrossRef] [PubMed]

4. Marra, I.F.S.; de Castro, P.P.; Amarante, G.W. Recent Advances in Azlactone Transformations. *Eur. J. Org. Chem.* **2019**, *2019*, 5830–5855. [CrossRef]

5. Almalki, A.J.; Ibrahim, T.S.; Taher, E.S.; Mohamed, M.F.A.; Youns, M.; Hegazy, W.A.H.; Al-Mahmoudy, A.M.M. Synthesis, Antimicrobial, Anti-Virulence and Anticancer Evaluation of New 5(4H)-Oxazolone-Based Sulfonamides. *Molecules* **2022**, *27*, 671. [CrossRef] [PubMed]

6. Mariappan, G.; Saha, B.P.; Datta, S.; Kumar, D.; Haldar, P.K. Design, synthesis and antidiabetic evaluation of oxazolone derivatives. *J. Chem. Sci.* **2011**, *123*, 335–341. [CrossRef]

7. Rodrigues, C.A.B.; Martinho, J.M.G.; Afonso, C.A.M. Synthesis of a Biologically Active Oxazol-5-(4H)-one via an Erlenmeyer–Plöchl Reaction. *J. Chem. Educ.* **2015**, *92*, 1543–1546. [CrossRef]

8. Mesaik, M.A.; Rahat, S.; Khan, K.M.; Zia, U.; Choudhary, M.I.; Murad, S.; Ismail, Z.; Attaur, R.; Ahmad, A. Synthesis and immunomodulatory properties of selected oxazolone derivatives. *Bioorg. Med. Chem.* **2004**, *12*, 2049–2057. [CrossRef]

9. Shoji, T.; Ito, I. Azulene-Based Donor–Acceptor Systems: Synthesis, Optical, and Electrochemical Properties. *Chem. Eur. J.* **2017**, *23*, 16696–16709. [CrossRef]

10. Asao, T. Azulenic novel n-electronic compounds. *Pure Appl. Chern.* **1990**, *62*, 507–512. [CrossRef]

11. Shoji, T.; Ito, S. The Preparation and Properties of Heteroarylazulenes and Hetero-Fused Azulenes. *Adv. Heterocycl. Chem.* **2018**, *126*, 1–54. [CrossRef]

12. Waltman, R.J.; Argon, J.B. Electrically conducting polymers: A review of the electropolymerization reaction, of the effects of chemical structure on polymer film properties, and of applications towards technology. *Can. J. Chem.* **1986**, *64*, 76. [CrossRef]

13. Imisides, M.D.; John, R.; Riley, P.J.; Wallace, G.G. The Use of Electropolymerization to Produce New Sensing Surfaces: A Review Emphasizing Electrodeposition of Heteroaromatic Compounds. *Electroanalysis* **1991**, *3*, 879–889. [CrossRef]

14. Sharma, N.; Banerjee, J.; Shrestha, N.; Chaudhury, D. A review on oxazolone, it' s method of synthesis and biological activity. *Eur. J. Biomed. Pharm. Sci.* **2015**, *2*, 964–987. Available online: https://www.researchgate.net/publication/280882247 (accessed on 26 January 2023).

15. Ghazvini Zadeh, E.H.; Tang, S.; Woodward, A.W.; Liu, T.; Bondar, M.V.; Belfield, K.D. Chromophoric Materials Derived from a Natural Azulene: Syntheses, Halochromism and One-Photon and Two-Photon Microlithography. *J. Mater. Chem. C* **2015**, *3*, 8495. [CrossRef]

16. Koch, M.; Blacque, O.; Venkatesan, K.; Mater, J. Impact of 2,6-connectivity in azulene: Optical properties and stimuli responsive behavior. *J. Mater. Chem. C* **2013**, *1*, 7400. [CrossRef]

17. Ito, S.; Morita, N. Creation of Stabilized Electrochromic Materials by Taking Advantage of Azulene Skeletons. *Eur. J. Org. Chem.* **2009**, *27*, 4567–4579. [CrossRef]

18. Tsurui, K.; Murai, M.; Ku, S.-Y.; Hawker, C.J.; Robb, M.J. Modulating the Properties of Azulene-Containing Polymers throughControlled Incorporation of Regioisomers. *Adv. Funct. Mater.* **2014**, *24*, 7338–7347. [CrossRef]

19. Wang, X.; Kok-Peng Ng, J.; Jia, P.; Lin, T.; Mui Cho, C.; Xu, J.; Lu, X.; He, C. Synthesis, Electronic, and Emission Spectroscopy, and Electrochromic Characterization of Azulene-Fluorene Conjugated Oligomers and Polymers. *Macromolecules* **2009**, *42*, 5534–5544. [CrossRef]

20. Amir, E.; Amir, R.J.; Campos, L.M.; Hawker, C.J. Stimuli-Responsive Azulene-Based Conjugated Oligomers with Polyaniline-like Properties. *J. Am. Chem. Soc.* **2011**, *133*, 10046–10049. [CrossRef]

21. Cristea, M.; Bîrzan, L.; Dumitrascu, F.; Enache, C.; Tecuceanu, V.; Hanganu, A.; Draghici, C.; Deleanu, C.; Nicolescu, A.; Maganu, M.; et al. 1-Vinylazulenes with Oxazolonic Ring-Potential Ligands for Metal Ion Detectors; Synthesis and Products Properties. *Symmetry* **2021**, *13*, 1209. [CrossRef]

22. Birzan, L.; Cristea, M.; Draghici, C.C.; Tecuceanu, V.; Maganu, M.; Hanganu, A.; Arnold, G.-L.; Ungureanu, E.-M.; Razus, A.C. 1-vinylazulenes–potential host molecules in ligands for metal ion detectors. *Tetrahedron* **2016**, *72*, 2316. [CrossRef]

23. Iftime, G.; Lacroix, P.G.; Nakatani, K.; Razus, A.C. Push-pull azulene-based chromophores with nonlinear optical properties. *Tetrahedron Lett.* **1998**, *39*, 6853. [CrossRef]

24. Asato, A.E.; Liu, R.S.H.; Rao, V.P.; Cai, Y.M. Azulene-containing donor-acceptor compounds as second-order nonlinear chromophores. *Tetrahedron Lett.* **1996**, *37*, 419–422. [CrossRef]

25. Anastasoaie, V.; Omocea, C.; Enache, L.-B.; Anicai, L.; Ungureanu, E.-M.; van Staden, J.F.; Enachescu, M. Surface Characterization of New Azulene-Based CMEs for Sensing. *Symmetry* **2021**, *13*, 2292. [CrossRef]

26. Krishna, D.N.G.; Philip, J. Review on surface-characterization applications of X-ray photoelectron spectroscopy (XPS): Recent developments and challenges. *Appl. Surf. Sci. Adv.* **2022**, *12*, 100332. [CrossRef]

27. Cernescu, A.; Szuwarzyński, M.; Kwolek, U.; Wydro, P.; Kepczynski, M.; Zapotoczny, S.; Nowakowska, M.; Quaroni, L. Label-Free Infrared Spectroscopy and Imaging of Single Phospholipid Bilayers with Nanoscale Resolution. *Anal. Chem.* **2018**, *90*, 10179–10186. [CrossRef] [PubMed]

28. Grossmann, L.; King, B.T.; Reichlmaier, S.; Hartmann, N.; Rosen, J.; Heckl, W.M.; Björk, J.; Lackinger, M. On-surface photopolymerization of two-dimensional polymers ordered on the mesoscale. *Nat. Chem.* **2021**, *13*, 730–736. [CrossRef] [PubMed]